Field Measurement and Analysis of Frequency and RoCoF for Low-Inertia Power Systems

He Yin ⬡ , *Senior Member, IEEE*, Wei Qiu ⬡ , *Member, IEEE*, Yuru Wu ⬡ , *Student Member, IEEE*,
Shutang You ⬡ , *Member, IEEE*, Jin Tan ⬡ , *Senior Member, IEEE*, Andy Hoke ⬡ , *Senior Member, IEEE*,
Cameron J. Kruse ⬡ , *Member, IEEE*, Brad W. Rockwell *, Member, IEEE*, and Yilu Liu ⬡ , *Fellow, IEEE*

Abstract—The frequency measurement and rate of change of frequency (RoCoF) calculations are important for active power, frequency control, and frequency-related protection in power system operations. With the rapid decrease in inertia under modern power systems, however, multiple power variations introduced by variable renewable energy bring large RoCoF and introduce oscillations in frequency measurements. To shed light on this issue, this article proposes a frequency measurement and RoCoF analysis technology, as well as the sensitivity analysis for the real low-inertia power grid. First, a real-world event in an island power grid is analyzed as an example, and an event numerical model is estimated considering four uncertainties, including event RoCoF, oscillation magnitude, oscillation frequency, and underfrequency load-shedding threshold. Then, a sensitivity analysis is performed using the Sobol indices method and quasi-Monte Carlo simulations to identify the dominant uncertainties based on the event model. The dominant uncertainties are compared to provide a guideline for the frequency estimation algorithm selection under different event cases. This algorithm is compared with an enhanced zero-crossing algorithm and gives a 3.41% better RoCoF error rate. Finally, an experiment is conducted using universal grid analyzers to validate the simulation results and the theoretical analysis.

Index Terms—Frequency measurement, low-inertia grid, rate of change of frequency (RoCoF), sensitivity analysis.

I. INTRODUCTION

THANKS to fast technology developments, distributed energy resources (DERs) and inverter-based resources (IBRs) are widely deployed in different kinds of power grids [1], making the load-generation balance more volatile. This is exacerbated if the inertia of the power grid is low, such as in an island grid. For example, the plan for the Hawaiian Islands is to use 100% renewable energy by the year 2045 [2], and most of that energy is expected to come from IBRs and DERs. The deployment of IBRs and DERs will further decrease the system inertia. This will cause fast frequency drops and higher rates of change of frequency (RoCoF) [3] during frequency events, such as a sudden generator trip. The IBRs will play a critical role in the fast frequency response and frequency-related protection, such as underfrequency load shedding, in the future power grid [4]. In addition, battery energy storage systems (BESSs) are being installed at multiple locations. These BESSs will participate in the frequency control by applying droop controls [5] or other methods, but the time delay and coordination among BESSs could cause frequency oscillations [6], which would lead to a reduced calculation accuracy of the RoCoF.

To support these functions, the precise measurement and fast-response capabilities of frequency and RoCoF are the keys to preventing the false detection and tripping caused by inaccurate measurements. An example is the Blue Cut Fire event that happened in California, where the frequency measurements triggered an erroneous trip [7]. IEEE standard 60255-118-1 [8] provides measurement performance requirements, but there is no specified algorithm for frequency measurements. Zero-crossing-based algorithms are basic algorithms that calculate the frequency by measuring the time duration of cycles [9]. A phase-locked loop (PLL) is another well-known technology to calculate the frequency in synchronized phasor measurements [10]; however, the performances of both zero-crossing and PLL-based algorithms suffer from the noise and transient factors in the power system. Discrete Fourier transform (DFT)-based algorithms have a relatively low computational requirement for frequency estimation [11]. DFT-based algorithms can be further improved by solving the off-nominal conditions [12], [13] and widening the frequency measurement range [14]. In a low-inertia

power system, both fast frequency dropping and oscillations exist as a result of the high proportion of DERs. But the tradeoffs between the fast frequency dropping speed and the frequency measurement accuracy in low-inertia power systems pose a new challenge to the selection of window parameters of the DFT method.

Precise measurements of RoCoF are critical for low-inertia power systems for applications including real-time system inertia estimation, fast frequency control, and event detection [15]. Based on this consideration, RoCoF is a fundamental measurement for phasor measurement units (PMUs), as listed in [8]. RoCoF is also a common measurement for other power system sensors, such as digital fault recorders (DFRs) and relays; however, most of these sensors calculate RoCoF by simply using two adjacent frequency measurements. To precisely measure RoCoF, some RoCoF estimation algorithms have been proposed that can be categorized into instantaneous and window-based algorithms.

For instantaneous algorithms, Romano and Paolone [16] introduce an enhanced interpolated DFT-based RoCoF measurement algorithm, and Derviškadić et al. [17] introduce an iterative interpolated DFT-based algorithm. Both use two adjacent frequency measurements to calculate the instantaneous RoCoF. The benefit of instantaneous algorithms is the low response time, but the accuracy of the RoCoF measurement is relatively low. In contrast, window-based algorithms use a set of frequency measurements to more accurately estimate the RoCoF. Wright et al. [18] use a phase step correction algorithm to remove the frequency spikes, thus increasing the RoCoF measurement accuracy. Singh and Pal [19] apply a DFT-based frequency measurement algorithm and then use a Kalman filter to increase the RoCoF measurement accuracy. A low-pass filter is implemented on the RoCoF measurements to obtain a smooth RoCoF measurement curve in [20]. Furthermore, a Taylor–Fourier model is used to calculate accurate RoCoFs in [21]. The window size of window-based algorithms is another interesting topic and a critical factor for RoCoF calculation. In [22], the recommended window size is from 0.1 to 0.5 s for power systems with large inertia. A small window, such as 0.1 s, is usually selected for microgrids or power systems with low inertia [23]. However, targeting on the RoCoF used in inertia estimation applications, the window size of the frequency calculation algorithm can be larger to reduce the disturbance from oscillations and enhance the measurement robustness.

These methods above are mainly applied to power grids with large inertia; however, it is challenging to accurately measure both the real-time frequency and RoCoF in low-inertia power systems because the frequency can drop quickly and has serious oscillations. Additionally, for frequency control and protection applications, the RoCoF calculation needs to be finished before the frequency reaches the underfrequency load-shedding threshold. Importantly, the inconsistency of control can cause oscillations and noises in frequency measurements, which can lead to disturbances and thus add difficulty to the frequency and RoCoF calculations. One of the critical parameters for both the frequency and RoCoF calculation algorithm is the window size selection. In a low inertia power system, its fast frequency dropping requires short window size algorithms while the frequency

oscillations require long window size algorithms. The existing frequency and RoCoF estimation algorithms discussed above have not fully considered the tradeoffs among the frequency response time, accuracy, and robustness against oscillations. To the best of our knowledge, there is a lack of a thorough discussion on the frequency and RoCoF calculation algorithms from the aspect of the window size design in low-inertia power systems with high deployments of IBRs and BESSs.

This article proposes a sensitivity analysis to address the optimal frequency measurement algorithm and find the dominant uncertain factor for both frequency and RoCoF calculations. The contributions of this article are summarized as follows.

1) An analysis is conducted on a real-world generation trip event that occurred within an island power system. In order to accurately represent this event, an event numerical model is developed, accounting for four uncertainties: a) event RoCoF, b) time-varying oscillation magnitude, c) oscillation frequency, and d) underfrequency load-shedding threshold.

2) In order to determine an appropriate window size and effectively balance the uncertainties, a sensitivity analysis is proposed utilizing the Sobol indices method in conjunction with quasi-Monte Carlo technologies.

3) To validate the effectiveness of the proposed method, an experimental test bench is established using two universal grid analyzers and an Omicron power source. A series of comparative experiments are conducted under various conditions, including different cycles, noise levels, parameters of the numerical event model, and frequency calculation methods.

The rest of the article is organized as follows. Section II presents real-world events. Then, the frequency and RoCoF measurement algorithms are proposed in Section III. The sensitivity analysis is conducted in Section IV. Hardware experiments are introduced in Section V. Finally, Section VI concludes this article.

II. REAL-WORLD EVENT ANALYSIS

Island power systems usually have low system inertia limited by the size of the island. Deployment of IBRs, such as photovoltaics, will further reduce the system inertia, which could result in a very high RoCoF during frequency events. In addition, some IBRs, such as BESSs, with fast frequency support functions, might try to inject power into the power systems when the frequency is lower than a predefined threshold, which could cause a frequency oscillation if the cooperation among multiple BESSs is not well designed.

A. Real-World Events

A real-world event recorded by DFRs is shown in Fig. 1 on Kauai Island on November 21, 2021 [24]. It is a major generation trip event (more than 60% of instantaneous generators tripped) for a 60-MW-scale power system. The event was confirmed by utility DFR data in four locations and one UGA throughout the island. This event is the most serious generation trip event in the year 2021 on Kauai Island where both the oscillation magnitude
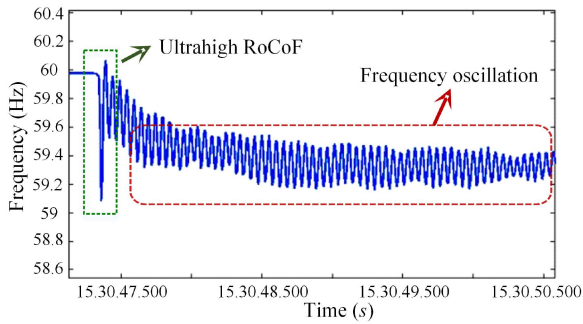
Fig. 1. Real-world frequency event from an island power system.

TABLE I
REAL-WORLD EXAMPLE EVENT INFORMATION

Event information	Value/descriptions
Location	Kauai Island
Power system scale	60 MW
Event type	Major generation trip
Time	Nov. 21, 2021
Maximum RoCoF	15 Hz/s
BESS injection frequency	59.85 Hz
Oscillation frequency	19–20 Hz
Oscillation magnitude	0.3 Hz
Underfrequency load-shedding frequency	59.2 Hz

and frequency dropping speed are the highest. The detailed event information can be found in Table I.

As shown in Fig. 1, at the very beginning of this event, there is a fast frequency drop caused by a generation trip, which is marked by the green rectangle. The maximum event RoCoF is observed to be roughly 15 Hz/s. Then, a frequency oscillation (outlined in red) can be observed during the frequency recovery stage, which is believed to be caused by the BESS power injection from multiple plants after the generation trip event. The oscillation frequency is between 19 and 20 Hz, and the largest oscillation magnitude is approximately 0.3 Hz. This oscillation lasts for more than 1 min at nearly constant amplitude (only 3 s are shown here), which brings challenges to the calculation of the RoCoF.

At the initial part of the frequency drop, a BESS power injection can be observed at approximately 59.85 Hz. This value can be different depending on the setting of the BESS controllers. Even though this event is a major generation trip event, it did not trigger significant underfrequency load shedding (the threshold frequency is 59.2 Hz for a 5-cycle duration) because of the fast responses from the BESSs. In the meantime, the BESS power injection also caused frequency oscillations.

B. Event Numerical Modeling

The motivation for establishing the numerical general event model is to simulate a wider range of event scenarios based on the available information from island events in low-inertia power systems. The targeted events primarily involve generation trips and load shedding, both of which are critical and commonly encountered. According to the real generation trip event discussed

in Section II-A, characterized by both RoCoF and frequency oscillations, it is essential to incorporate these aspects into the model. The voltage waveform of the event within a 5-s interval can be represented as a discrete-time signal with a sampling rate f_s, expressed by the following equation:

$$\mathrm{Sig}[n] = \sqrt{2}V_{\mathrm{amp}}\cos(a[n])$$

$$a[n] = \begin{cases} a[n-1] + \frac{2\pi f_0}{f_s}, & \text{if } n <= n_s \\ a[n-1] + \frac{2\pi f_e}{f_s}, & \text{if } n > n_s \end{cases}$$

$$f_e = f_0 \pm M_f \sin\left[\frac{2\pi f_{\mathrm{osc}}(n-n_s)}{f_s}\right] \pm \Delta f$$

$$\Delta f = \frac{\mathrm{RoCoF}}{f_s} \tag{1}$$

where V_{amp} denotes the voltage magnitude, $a[n]$ represents the voltage phase at discrete time n (with $a[0]$ initialized as 0), f_0 corresponds to the nominal frequency, f_e denotes the frequency following the event occurrence, n_s signifies the event starting time (constrained between 0 and 5 s), M_f is the time-varying frequency magnitude of the oscillation, f_{osc} denotes the oscillation frequency, Δf represents the frequency change after the event, and RoCoF represents the RoCoF value during the event, excluding the oscillatory component. In the subsequent analysis, the oscillation frequency is considered part of the ground truth frequency, although the ground truth RoCoF value does not take the frequency oscillation into account, as the focus lies on estimating the inertia. Besides, the magnitude M_f and the frequency change Δf can be settled as zero to model the generation trips, load shedding, or oscillation component, respectively.

III. FREQUENCY AND ROCOF CALCULATION

A. Frequency Calculation

The frequency calculation algorithm is a critical point for RoCoF estimation. Among existing frequency calculation algorithms, DFT-based algorithms are the most commonly used [25]; however, different computation windows of the phasor angle will influence the frequency estimation. To address this issue, a recursive DFT-based frequency estimation algorithm is proposed.

According to the voltage/current signals in (1), the phasor can be calculated in a recursive DFT method [26]

$$\overline{X(t)} = \frac{1}{\sqrt{2}}\left[X_c(t) + jX_s(t)\right]$$

$$\varphi(t) = \tan^{-1}\frac{-X_s(t)}{X_c(t)}$$

$$X_c(t) = \frac{2}{N}\sum_{k=t-N}^{t}\mathrm{Sig}(k)\cos\left(\frac{2\pi}{N}k\right)$$

$$X_s(t) = \frac{2}{N}\sum_{k=t-N}^{t}\mathrm{Sig}(k)\sin\left(\frac{2\pi}{N}k\right) \tag{2}$$

where $\overline{X(t)}$ is the DFT of the voltage/current signals, N stands for the number of samples per cycle, and t is the time stamp, the $X_c(t)$ and $X_s(t)$ are the real and imaginary parts, respectively.

To reduce the calculation burden, a recursive method is used to update the voltage/current phasor

$$X_c(t+1) = X_c(t) + \frac{2}{N}[\text{Sig}(t+1) - \text{Sig}(t+1-N)]$$
$$\cos\left(\frac{2\pi}{N}t\right)$$
$$X_s(t+1) = X_s(t) + \frac{2}{N}[\text{Sig}(t+1) - \text{Sig}(t+1-N)]$$
$$\sin\left(\frac{2\pi}{N}t\right). \tag{3}$$

To obtain the frequency, the fitting method is used. Assuming the voltage/current phasor angle varies following a quadratic function:

$$\varphi(t) = a_0 + a_1 t + a_2 t^2 \tag{4}$$

where a_0 to a_2 are coefficients. The primary reason for utilizing the quadratic function (second-order polynomial function) is to decrease the estimated frequency error because the real-world phase angles are actually nonlinear functions as a result of noises, oscillations, and disturbances [27]. Given a phasor computation window of M, the phasor angles in the window can be used to calculate a_0 to a_2 as

$$\varphi = \begin{bmatrix} 1 & 1 & 1 \\ 1 & 2 & 2^2 \\ \vdots & \vdots & \vdots \\ 1 & M & M^2 \end{bmatrix} \begin{bmatrix} a_0 \\ a_1 \\ a_2 \end{bmatrix}. \tag{5}$$

By using the least-squares error solution, a_0 to a_2 can be calculated. In this way, the frequency can be estimated as

$$f = f_0 + \frac{1}{2\pi} N f_0 (a_1 + 2a_2 N f_0 t) \tag{6}$$

where t is the time instant for the frequency.

B. RoCoF Calculation

After estimating the frequency, the RoCoF is commonly calculated by using the frequency difference in the two adjacent estimated frequencies in PMUs; however, this RoCoF cannot represent the true RoCoF when the event occurs.

In an island power system with low inertia, the frequency can drop very quickly after the loss of a generator. For example, the frequency dropped from 60 to 59.1 Hz within 50 ms in the event shown in Fig. 1. Because there is a predefined underfrequency load-shedding threshold, the frequency measured after this threshold could be invalid for RoCoF estimation purposes because the load shedding already happened, and thus, a fixed RoCoF estimation window becomes meaningless. An accurate RoCoF should be calculated using the measured frequency before reaching the underfrequency load-shedding threshold.

To calculate the most accurate RoCoF for a given event, the starting point of the RoCoF is fixed at the beginning of the event, and the ending point of the RoCoF can be located at the underfrequency load-shedding threshold. This choice makes the most of the very short time window available to obtain a reliable RoCoF value in low-inertia power systems.

Furthermore, to improve the RoCoF estimation accuracy, a first-order least-squares error method is used for the curve fitting with frequency measurements. First, the frequency is assumed to be represented as follows:

$$f(t) = b_0 + b_1 t \tag{7}$$

where b_0 and b_1 are the intercept and slope coefficients, respectively. The objective is to calculate b_1, which is actually the RoCoF. Given the K frequency measurements in the computation window, the frequency can be represented as

$$f = Kb = \begin{bmatrix} 1 & 1 \\ 1 & 2 \\ \vdots & \vdots \\ 1 & K \end{bmatrix} \begin{bmatrix} b_0 \\ b_1 \end{bmatrix} \tag{8}$$

where b_i can be calculated as

$$b = \left[K^T K\right]^{-1} K^T f. \tag{9}$$

Because $\left[K^T K\right]^{-1} K^T$ depends on the starting and the ending points of the RoCoF window, it can vary with different events. Then, the RoCoF can be derived from b. The advantage of the RoCoF calculation is that it can be implemented in the embedded device firmware.

IV. SENSITIVITY ANALYSIS

The robustness of the proposed method is critical for practical applications. To verify the uncertainty under a range of frequency event characteristics, a sensitivity analysis is performed to quantitatively study the influences of various event parameters and determine the dominant parameters.

The window size of the DFT-based method is an important parameter that determines the accuracy of the frequency measurement. To determine the optimal frequency estimation algorithm and window size (M), the window size of the DFT-based algorithm varied from 1 to 6 ac line cycles (e.g., 1/60 s to 0.1 s in U.S. power grids.).

In addition to the window size, other uncertainties in this sensitivity analysis are the event RoCoF, the oscillation magnitude, the oscillation frequency, and the underfrequency load-shedding threshold. The analyzed range of these four uncertainties is determined based on the real-world event discussed in Section II, as listed in Table II. The real-world event is considered as the serious case in this study so that its parameters are considered as the upper limits. They are named from S1 to S4, and the cycle number of the window size is an integer uncertainty that will be analyzed separately. The distributions of the uncertainties are assumed to be uniform.

Based on the frequency and RoCoF estimation algorithm discussed in Section III, a nonlinear relationship exists between the uncertainties and the estimated measurements, frequency, and RoCoF.

TABLE II
RANGES OF PARAMETERS INFLUENCING UNCERTAINTY

Uncertainties	Lower boundary	Higher boundary	Index
Event RoCoF (Hz/s)	1	15	S1
Oscillation magnitude (Hz)	0	0.3	S2
Oscillation frequency (Hz)	0	20	S3
Underfrequency load-shedding threshold (Hz)	58.5	59.5	S4
Window size for frequency estimation (cycle)	1	6	NaN

To reveal this relationship, a variation-based Sobol method [28] is used in this article for a global sensitivity analysis. The sensitivity coefficients, i.e., Sobol indices, are used to represent the amount of variance of uncertainty to the total variance. The quasi-Monte Carlo algorithm with quasi-random samples is adopted to estimate the first-order Sobol indices because of its faster convergence speed. The frequency measurement reporting rate is assumed to be 120 Hz based on the IEEE C37.118.1 2018 [8].

To evaluate the calculation performances, two different kinds of indexes are established as the target of the sensitivity analysis: 1) the frequency error, Freq_{err}, and 2) the RoCoF error, $\text{RoCoF}_{\text{err}}$. They are calculated as

$$\text{Freq}_{\text{err}} = \mid \text{Freq}_{\text{est}} - \text{Freq}_{\text{ref}} \mid$$
$$\text{RoCoF}_{\text{err}} = \mid \text{RoCoF}_{\text{est}} - \text{RoCoF}_{\text{ref}} \mid \qquad (10)$$

where Freq_{est} and $\text{RoCoF}_{\text{est}}$ are the frequency and RoCoF estimated by the DFT-based algorithm and curve fitting, and Freq_{ref} and $\text{RoCoF}_{\text{ref}}$ are the frequency and RoCoF references predefined in the simulated event models listed in (1). Because the target for the frequency is to precisely measure the dynamic frequency, whereas the target for the RoCoF is to estimate the inertia, Freq_{ref} is defined as the frequency considering oscillations, whereas $\text{RoCoF}_{\text{ref}}$ is defined as the RoCoF without oscillations. To justify the performance of the estimated RoCoF, a better frequency estimation algorithm should have both a low Freq_{err} and a low $\text{RoCoF}_{\text{err}}$.

A. First-Order Sensitivity Indices

The first-order Sobol indices under different DFT window sizes are illustrated graphically in Figs. 2 and 3, respectively. A larger Sobol sensitivity indicates a larger effect of the parameter on the measurement uncertainty. Note that the underfrequency load-shedding threshold (S4) is not used in the frequency error calculation.

It can be observed that S1 and S2 have the dominant Sobol sensitivities among the four parameters studied. In addition, S1 increases when the DFT window size increases. In contrast, S2 decreases when the DFT window size increases. This is understandable because when the DFT window size increases, the algorithm becomes more robust against the oscillation and more sensitive toward the event RoCoF for both frequency and RoCoF errors.
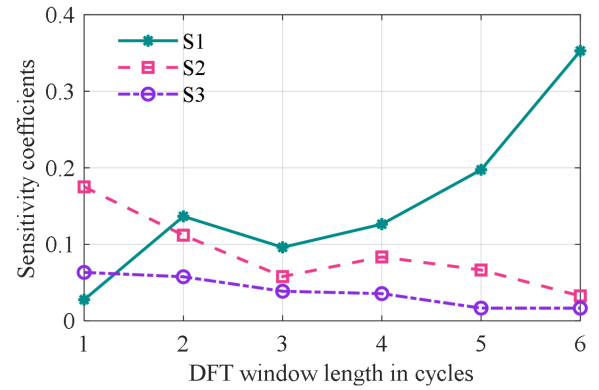

Fig. 2.   First-order Sobol indices for the frequency error under different DFT window sizes.
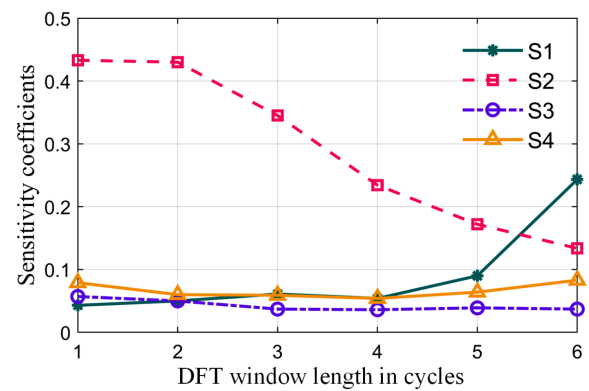

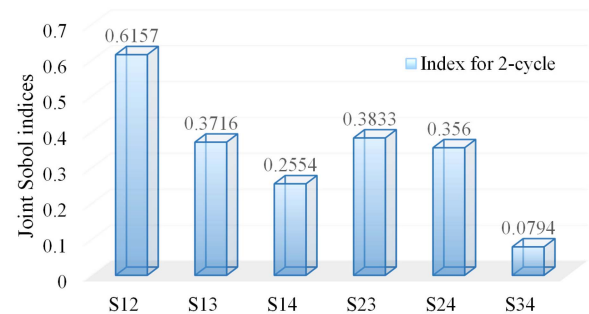Fig. 3.   First-order Sobol indices for the RoCoF error under different DFT window sizes.

Fig. 4.   Joint Sobol indices for 2-cycle DFT-based frequency estimation algorithm.

B. Second-Order Sensitivity Indices

As illustrated in Figs. 2 and 3, S1 and S2 are the two dominant uncertainties resulting from their large values among the first-order Sobol indices. To further verify this, the joint Sobol indices for every two uncertainties (e.g., S12 means the joint Sobol indices for S1 and S2) for the 2- and 6-cycle DFT-based algorithms are illustrated in Figs. 4 and 5, where the RoCoF error is used as the target.

As shown in Figs. 4 and 5, S12 is much larger than the other joint Sobol indices for the 2-cycle DFT-based algorithm,
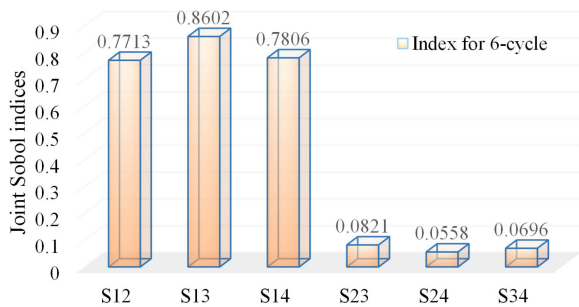
Fig. 5. Joint Sobol indices for 6-cycle DFT-based frequency estimation algorithm.

whereas S12, S13, and S14 are larger than the other joint Sobol indices for the 6-cycle DFT-based algorithm. This result matches the illustrations in Figs. 2 and 3. Because S12 is relatively large for both algorithms, a more detailed study on these two uncertainties, i.e., S1 and S2, is given using 2- and 6-cycle DFT-based algorithms. During this study, the S3 and S4 are set to their respective mean values within their range to ensure they do not influence the study.

To verify the frequency error, the performance of both the frequency and RoCoF measurements for 2- and 6-cycle DFT-based algorithms is presented in Fig. 6(a) and (b). The 2-cycle DFT-based algorithm has a better frequency measurement performance when the oscillation magnitude is high. In addition, it has a better RoCoF measurement performance when the event RoCoF is low and the oscillation magnitude is low. Additionally, the 6-cycle DFT-based algorithm gives a lower frequency error when the oscillation magnitude is low. Meanwhile, it has a very smooth overall performance for the RoCoF measurement error. This verifies that the 2-cycle DFT-based algorithm is more accurate for the instantaneous frequency measurement, whereas the 6-cycle DFT-based algorithm is more robust against oscillations and event RoCoF changes for the inertia-based RoCoF measurements.

To gain further insight from this figure, there is an intersection line between the two surfaces generated from the two algorithms. If Fig. 6(a) and (b) are reduced to 2-D versions, they clearly illustrate these intersection curves, as given in Fig. 6(c) and (d), where the green area shows where the 6-cycle DFT-based algorithm will have better performance, and the blue area indicates where the two-cycle DFT algorithm will be a better choice. As shown in these figures, the 2-cycle DFT algorithm will have a more precise frequency estimation if the oscillation magnitude is high, whereas it has a better RoCoF estimation if the event RoCoF reference value is very high because of the benefits of the short DFT window; however, the oscillation magnitude can have a large influence on the RoCoF estimation from the two-cycle DFT algorithm because the measured RoCoF can be the oscillation RoCoF instead of the true event RoCoF. On the other hand, the RoCoF estimation of the 6-cycle DFT algorithm is much more robust against the oscillation magnitude changes; however, the accuracy of the frequency estimation is reduced with a large oscillation magnitude as a result of the large DFT window size.

This can be an easy guideline for the end user to select the best-performing algorithm if they know the event RoCoF range and the oscillation magnitude range. Here, 2- and 6-cycle DFT-based algorithms are used because they represent typical window lengths for PMUs. The end user can also customize the algorithm window length by redrawing this figure.

C. Influence of Other Uncertainties

To further study the influence of S3 and S4 (oscillation frequency and underfrequency load-shedding threshold) on the performance surface, two cases are studied: 1) the oscillation frequency is increased from 10 to 15 Hz, and 2) the underfrequency load-shedding threshold is increased from 59 to 59.5 Hz. The RoCoF error is chosen as the performance target because S4 is only available for the RoCoF error.

In the first case, the 2-D versions of the performance surface for the 2- and 6- cycle DFT-based algorithms are shown in Fig. 6(e). This shows that the overall performance curves are similar to Fig. 6(d). By changing the oscillation frequency, the intersection curve shape changes. When the oscillation magnitude value is high, the 2-cycle DFT-based algorithm covers a larger area than the 6-cycle DFT-based algorithm.

In the second case, again, the 2-D version of the performance surface for the 2- and 6-cycle DFT-based algorithms is shown in Fig. 6(f). In contrast, by changing the underfrequency load-shedding threshold, the intersection curve changes in the opposite direction. In this case, when the underfrequency load-shedding threshold is high, the 2-cycle DFT-based algorithm covers a larger area than the 6-cycle DFT-based algorithm.

V. EXPERIMENTAL VALIDATION

A. Verification Through Hardware Test Bench

To verify the sensitivity analysis in Section III, a series of experiments were conducted. An experimental test bench is set up as illustrated in Figs. 7 and 8.

The Omicron power source is used to generate ideal synchronized voltage signals by using the global positioning system (GPS) and a timing source (SEK-2488 satellite-synchronized network clock). The voltage signal is using a frequency profile similar to the one in (1). Then, two UGAs [29] with 2- and 6-cycle DFT-based algorithms deployed are connected to the Omicron power source (256 plus) through a power strip. The UGAs are named UGA 1 and UGA 2. Note that these two UGAs can also provide high-speed synchrophasors, and they are connected to separate GPS units as well. They stream the synchrophasor measurements to the router and then directly to the server in real time. The data acquisition of UGAs is designed with 16-b ADC, 5760-Hz sampling rate, and antialiasing filters. Detailed UGA hardware design can be found in [29]. The primary reason for choosing 5760 Hz is that typically a rate of 48 samples per cycle is required to detect the fluctuations and this value should be an integer multiple of the fundamental frequency. A photo of this test bench is also shown in Fig. 8. The GPS, power strip, and router are not shown in this photo.
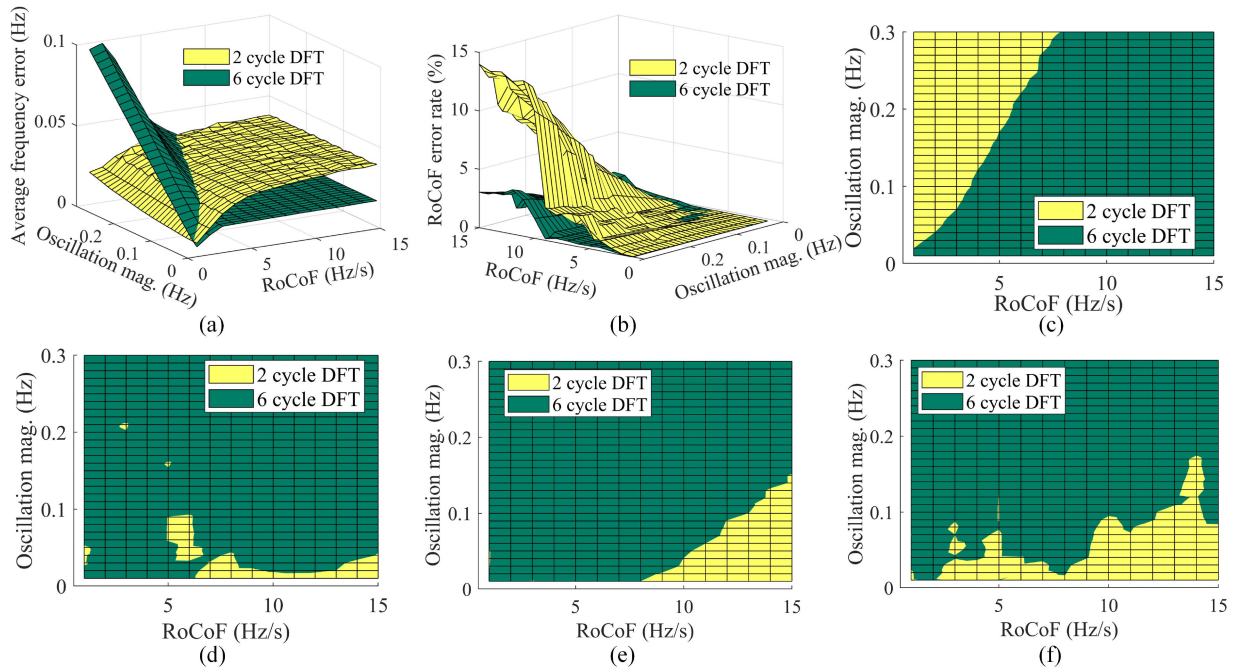
Fig. 6. Performance surfaces of frequency measurements and RoCoF measurements for 2- and 6-cycle DFT-based algorithms. (a) Performance surfaces of frequency measurements. (b) Performance surfaces of RoCoF measurements. (c) 2-D version of the best-performing algorithm surface of frequency measurements for 2- and 6-cycle DFT-based algorithms. (d) 2-D version of the best-performing algorithm surface of RoCoF measurements for 2- and 6-cycle DFT-based algorithms. (e) 2-D version of the best-performing algorithm surface for 2- and 6-cycle DFT-based algorithms under case one. (f) 2-D version of the best-performing algorithm surface for 2- and 6-cycle DFT-based algorithms under case two.
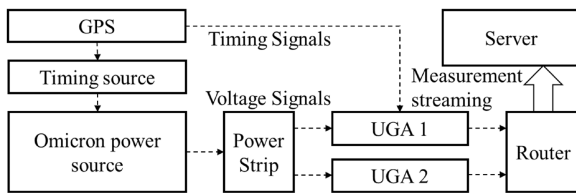
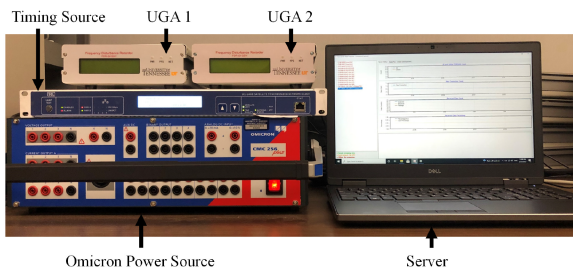Fig. 7. Experiment test bench setup schematic.

Fig. 8. Experiment test bench setup.

Because it is time-consuming to verify the entire performance curves shown in Fig. 6, four test points are selected from Fig. 6(b), which are located at four corners. For each test point, the oscillation frequency and underfrequency load-shedding threshold are set as 10 and 59 Hz, respectively. The measured frequency traces for each of the four tests under both 2- and 6-cycle DFT-based methods are illustrated in Fig. 9. The measured frequencies verify that the 2-cycle DFT-based method

can precisely measure the frequency oscillations and the 6-cycle DFT-based method can precisely measure RoCoFs.

Because there are only four points per surface, the non-linear dynamics cannot be fully shown. The experimental results have been put together with the simulation curves in Fig. 10. This shows the experimental results basically match the simulation results, but there is an average 4.08% difference between the simulation and experiment that is caused by the nonidealities in the experiment, such as filters in the sampling circuit and the power signal accuracy. Through this comparison, the accuracy of the proposed sensitivity analysis has been verified.

B. Benchmarking Algorithm Comparison

To verify the performance of the proposed DFT-based algorithm, a comparison between an enhanced zero-crossing frequency estimation algorithm [30] and the 6-cycle DFT-based algorithm is given with the RoCoF error to be the target. The oscillation frequency is 10 Hz, the RoCoF is 1 Hz/s, and the underfrequency load-shedding threshold is 59 Hz for this comparison. Note that both algorithms are using the first-order least-squares error method to calculate the RoCoF from the frequency. As illustrated in Fig. 11, the RoCoF error rate of the DFT-based algorithm is lower than that of the enhanced zero-crossing one from different oscillation magnitude cases. RoCoF$_{erate}$ is calculated as

$$\mathrm{RoCoF_{erate}} = \left| \frac{\mathrm{RoCoF_{est}} - \mathrm{RoCoF_{ref}}}{\mathrm{RoCoF_{ref}}} \right|. \tag{11}$$
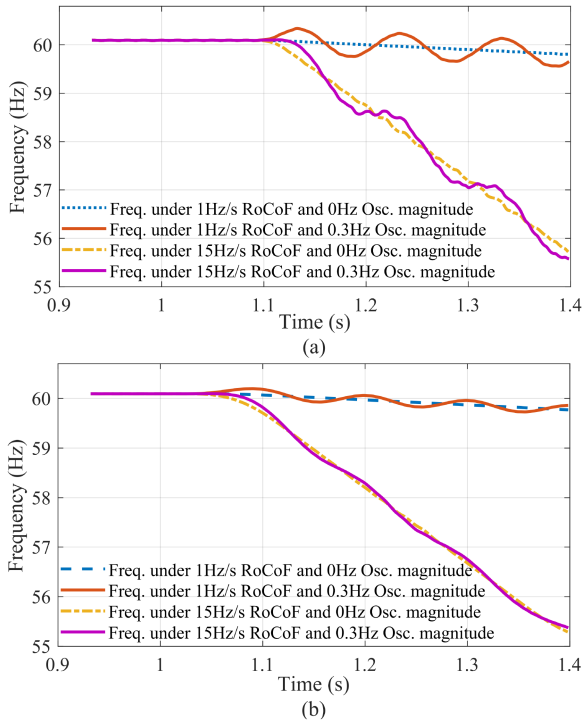
Fig. 9. (a) Frequency measurement under 2-cycle DFT method. (b) Frequency measurement under 6-cycle DFT method.
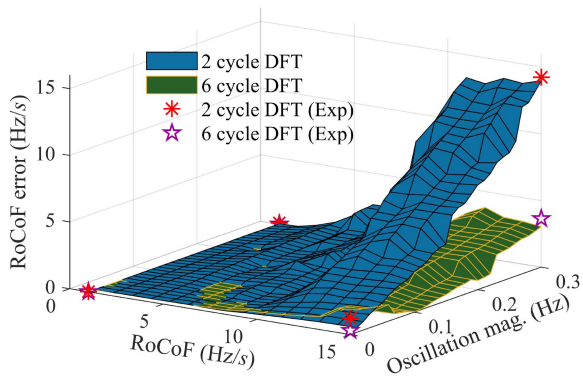

Fig. 10. Experimental validation with 2- and 6-cycle DFT-based algorithms.
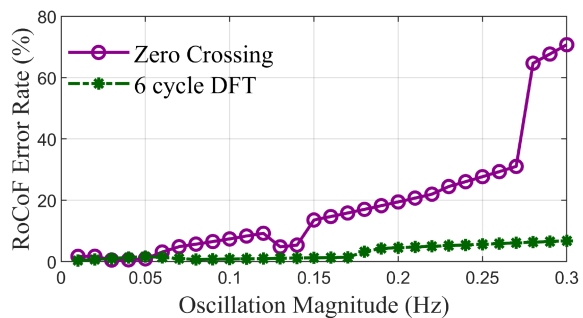

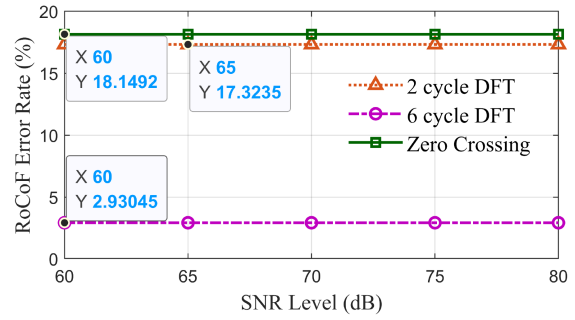Fig. 11. Algorithm comparison between zero-crossing and 6-cycle DFT methods.

Fig. 12. RoCoF error rate under different SNR levels.

The average error rate from the 6-cycle DFT is 3.41% better than the enhanced zero-crossing algorithm. The main reason is that the magnitude of the oscillation will affect the accuracy of the zero-crossing point, thereby introducing calculation errors.

C. Influence of Noise Levels

Another source of uncertainty in the frequency and RoCoF measurements is the noise level in the sampled voltage or current waveform. In most PMU devices, there will be hardware or software filters to reduce the noise level; however, minor noise on the sampled waveform will still influence the frequency and RoCoF estimations. The noise level has not been added to the uncertainties in the sensitivity analysis because noise on waveforms is a common uncertainty for all situations, which is not unique for events from low-inertia power systems.

To study the influence of the noise level, white noise from a 60- to 80-dB signal-to-noise ratio (SNR) has been added to the event model in (1). Note that the noise level used is a common SNR range for power grids. It has a relatively low SNR value when the power grid size becomes smaller. Again, the RoCoF error is used as the performance target. Fig. 12 illustrates the average RoCoF$_{erate}$ for three algorithms under different noise levels, where the RoCoF is 1 Hz/s, the oscillation is 10 Hz, the oscillation magnitude is 0.15 Hz, and the underfrequency load-shedding threshold is 59 Hz, showing a clear conclusion that all three algorithms are not sensitive to noise levels.

D. Influence of Sampling Rate

The sampling rate utilized in this article is 5760 Hz, which is to be constant with the UGA hardware. However, the DFT-based frequency estimation algorithm is actually sensitive to the sampling rate. In order to illustrate the influence, Fig. 13 presents the frequency errors from two DFT-based algorithms under a 60-Hz grid signal with 60-dB noise among different sampling rates. It is very clear that a higher sampling rate can lead to a lower frequency error for both 2- and 6-cycle DFT-based algorithms. However, there exists an obvious tradeoff between the calculation burden increase and the decrease in error here.

VI. CONCLUSION

To enhance the measurement accuracy of frequency and RoCoF in low-inertia power systems, this article presented a
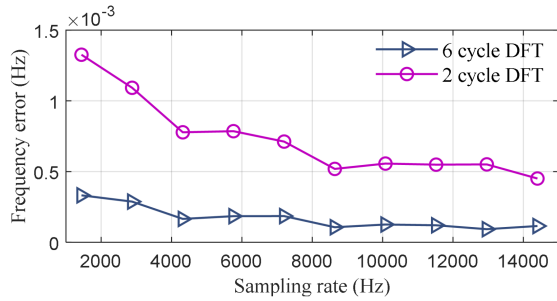
Fig. 13. Frequency error under different sampling rates with 2- and 6-cycle DFT-based algorithms.

real-time, optimal frequency, and RoCoF measurement algorithm and proposed the sensitivity analysis method for selecting the parameters. A field event from an island grid was treated as the starting point for a case study. An event numerical model was first designed and introduced based on a real-world event. Then, to study the dominant uncertainties in the event, a Sobol index and a quasi-Monte-Carlo-simulation-based sensitivity analysis with DFT-based algorithms were presented. From the results of the sensitivity analysis, it can be concluded that the 6-cycle DFT-based frequency estimation algorithm is more robust for RoCoF estimations of underfrequency oscillations, whereas the 2-cycle DFT-based frequency estimation algorithm has a more precise estimation for the instantaneous frequency estimations. The end user can choose their unique algorithm depending on the characteristics of the target events. Finally, an experiment with UGAs was conducted to verify the effectiveness of the proposed method in which the average error difference is only 4.08% between the theoretical analysis and the simulation results. By comparing the RoCoF estimation performance between the 6-cycle DFT-based frequency estimation algorithm and an enhanced zero-crossing algorithm, a 3.41% overall performance improvement was observed.

REFERENCES

[1] F. Adinolfi, G. M. Burt, P. Crolla, F. D'Agostino, M. Saviozzi, and F. Silvestro, "Distributed energy resources management in a low-voltage test facility," *IEEE Trans. Ind. Electron.*, vol. 62, no. 4, pp. 2593–2603, Apr. 2015, doi: 10.1109/TIE.2014.2377133.

[2] J. S. Hill, "Hawaii electric blows past 2020 target on road to 100% renewable energy," 2021. Accessed: Aug. 2023. [Online]. Available: https://reneweconomy.com.au/hawaii-electric-blows-past-2020-target-on-road-to-100-renewable-energy/

[3] M. Grebla, J. R. A. K. Yellajosula, and H. K. Høidalen, "Adaptive frequency estimation method for ROCOF islanding detection relay," *IEEE Trans. Power Del.*, vol. 35, no. 4, pp. 1867–1875, Aug. 2020.

[4] J. Ye, L. Liu, J. Xu, and A. Shen, "Frequency adaptive proportional-repetitive control for grid-connected inverters," *IEEE Trans. Ind. Electron.*, vol. 68, no. 9, pp. 7965–7974, Sep. 2021, doi: 10.1109/TIE.2020.3016247.

[5] J. W. Shim, G. Verbič, H. Kim, and K. Hur, "On droop control of energy-constrained battery energy storage systems for grid frequency regulation," *IEEE Access*, vol. 7, pp. 166353–166364, 2019.

[6] B. Qin, Y. Xu, C. Yuan, and J. Jia, "A unified method of frequency oscillation characteristic analysis for multi-VSG grid-connected system," *IEEE Trans. Power Del.*, vol. 37, no. 1, pp. 279–289, Feb. 2022.

[7] NERC, "1,200 MW fault induced solar photovoltaic resource interruption disturbance report," 2017. Accessed: Aug. 2023. [Online]. Available: https://www.nerc.com/pa/rrm/ea/1200_MW_Fault_Induced_Solar_Photovoltaic_Resource_/1200_MW_Fault_Induced_Solar_Photovoltaic_Resource_Interruption_Final.pdf

[8] *IEEE/IEC International Standard - Measuring Relays and Protection Equipment - Part 118-1: Synchrophasor for Power Systems - Measurements*, IEC/IEEE 60255-118-1:2018, pp. 1–78, 2018.

[9] Z. LiH. Liu, J. Zhao, T. Bi, and Q. Yang, "A power system disturbance classification method robust to PMU data quality issues," *IEEE Trans. Ind. Informat.*, vol. 18, no. 1, pp. 130–142, Jan. 2022.

[10] M. Karimi-Ghartemani, B.-T. Ooi, and A. Bakhshai, "Application of enhanced phase-locked loop system to the computation of synchrophasors," *IEEE Trans. Power Del.*, vol. 26, no. 1, pp. 22–32, Jan. 2011.

[11] J. Zhao, "Performance improvement of wide-area-monitoring-system (WAMS) and applications development," Ph.D. Elect. Eng. Comput. Sci., Univ. Tennessee, Knoxville, TN, USA, 2018.

[12] F. A. S. Neves, H. E. P. de Souza, F. Bradaschia, M. C. Cavalcanti, M. Rizo, and F. J. Rodriguez, "A space-vector discrete Fourier transform for unbalanced and distorted three-phase signals," *IEEE Trans. Ind. Electron.*, vol. 57, no. 8, pp. 2858–2867, Aug. 2010, doi: 10.1109/TIE.2009.2036646.

[13] D. Macii, D. Petri, and A. Zorat, "Accuracy analysis and enhancement of DFT-based synchrophasor estimators in off-nominal conditions," *IEEE Trans. Instrum. Meas.*, vol. 61, pp. 2653–2664, Oct. 2012, doi: 10.1109/TIM.2012.2199197.

[14] T. Xia and Y. Liu, "Single-phase phase angle measurements in electric power systems," *IEEE Trans. Power Syst.*, vol. 25, no. 2, pp. 844–852, May 2010.

[15] C. Li, Y. Yang, N. Mijatovic, and T. Dragicevic, "Frequency stability assessment of grid-forming VSG in framework of MPME with feedforward decoupling control strategy," *IEEE Trans. Ind. Electron.*, vol. 69, no. 7, pp. 6903–6913, Jul. 2022, doi: 10.1109/TIE.2021.3099236.

[16] P. Romano and M. Paolone, "Enhanced interpolated-DFT for synchrophasor estimation in FPGAs: Theory, implementation, and validation of a PMU prototype," *IEEE Trans. Instrum. Meas.*, vol. 63, no. 12, pp. 2824–2836, Dec. 2014.

[17] A. Derviškadić, P. Romano, and M. Paolone, "Iterative-interpolated DFT for synchrophasor estimation: A single algorithm for P- and M-class compliant PMUs," *IEEE Trans. Instrum. Meas.*, vol. 67, no. 3, pp. 547–558, Mar. 2018.

[18] P. S. Wright, P. N. Davis, K. Johnstone, G. Rietveld, and A. J. Roscoe, "Field measurement of frequency and ROCOF in the presence of phase steps," *IEEE Trans. Instrum. Meas.*, vol. 68, no. 6, pp. 1688–1695, Jun. 2019.

[19] A. K. Singh and B. C. Pal, "Rate of change of frequency estimation for power systems using interpolated DFT and Kalman filter," *IEEE Trans. Power Syst.*, vol. 34, no. 4, pp. 2509–2517, Jul. 2019.

[20] G. Frigo, A. Derviškadić, Y. Zuo, and M. Paolone, "PMU-based ROCOF measurements: Uncertainty limits and metrological significance in power system applications," *IEEE Trans. Instrum. Meas.*, vol. 68, no. 10, pp. 3810–3822, Oct. 2019.

[21] M. Bertocco, G. Frigo, C. Narduzzi, C. Muscas, and P. A. Pegoraro, "Compressive sensing of a Taylor-Fourier multifrequency model for synchrophasor estimation," *IEEE Trans. Instrum. Meas.*, vol. 64, no. 12, pp. 3274–3283, Dec. 2015.

[22] A. Arana et al., "Fast frequency response concepts and bulk power system reliability needs, in NERC inverter-based resource performance task force (IRPTF)," 2020.

[23] C. Zhang, X. Dou, Z. Zhang, G. Lou, F. Yang, and G. Li, "Inertia-enhanced distributed voltage and frequency control of low-inertia microgrids," *IEEE Trans. Power Syst.*, vol. 36, no. 5, pp. 4270–4280, Sep. 2021.

[24] S. Dong et al., "Analysis of November 21, 2021, Kaua'i Island power system 18-20 Hz oscillations," 2023, *arXiv:2301.05781*.
[25] H. Wen, C. Li, and L. Tang, "Novel three-point interpolation DFT method for frequency measurement of sine-wave," *IEEE Trans. Ind. Informat.*, vol. 13, no. 5, pp. 2333–2338, Oct. 2017.
[26] J. Chen, "Accurate frequency estimation with phasor angles," Virginia Tech, 1994. [Online]. Available: https://vtechworks.lib.vt.edu/handle/10919/46099
[27] L. Zhan, Y. Liu, J. Culliss, J. Zhao, and Y. Liu, "Dynamic single-phase synchronized phase and frequency estimation at the distribution level," *IEEE Trans. Smart Grid*, vol. 6, no. 4, pp. 2013–2022, Jul. 2015, doi: 10.1109/TSG.2015.2400973.
[28] I. Sobol, "Global sensitivity indices for nonlinear mathematical models and their Monte Carlo estimates," *Math. Comput. Simul.*, vol. 55, no. 1, pp. 271–280, 2001.
[29] H. Yin et al., "Low cost, flexible, and distribution level universal grid analyser platform: Designs and implementations," *IET Gener. Transmiss. Distrib.*, vol. 14, no. 19, pp. 3945–3952, 2020.
[30] W. Yao and J. E. A. Zhao, "Synchrophasor measurement method for power systems," Google Patents, 2018 US Patent App. 15/609,484, 2018.

Shutang You (Senior Member, IEEE) received the B.S. and M.S. degrees in electrical engineering from Xi-an Jiaotong University, Xi'an, China, in 2011 and 2014, respectively, and the Ph.D. degree in electrical engineering from The University of Tennessee, Knoxville, TN, USA, in 2017.

He was a Research Assistant Professor with the Department of Electrical Engineering and Computer Science from 2018 to 2021. He is currently an Engineer with EDP Renewables, Madrid, NM, USA. His research interests include power grid dynamics and monitoring.
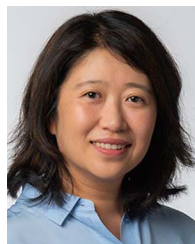
Jin Tan (Senior Member, IEEE) received the B.E. and Ph.D. degrees in electrical engineering from Southwest Jiaotong University, Chengdu, China, in 2007 and 2014, respectively.

From 2009 to 2011, she was a visiting Ph.D. Student with the Department of Energy Technology, Aalborg University, Denmark. In 2014, she was a Postdoctoral Researcher with the Department of Electrical Engineering and Computer Science, The University of Tennessee, Knoxville, TN, USA. In 2015, she joined National Renewable Energy Laboratory (NREL), Golden, CO, USA. She is currently a Principal Engineer with Power Systems Engineering Center, NREL. Her research interests include power system stability and control, multitimescale dynamic modeling of renewable generations, and energy storage for grid applications.

Dr. Tan was the Editor of the *International Transaction on Electrical Energy System*. She is a Member of the Power and Energy Society (PES) and IEEE Women in Engineering. She was the recipient of the President Award with National Renewable Energy Laboratory in 2018 and 2020, the NREL Outstanding Mentor Award in 2020, 2021, and 2022, and the Best Paper Award in 2016, 2018, 2019, and 2020.

He Yin (Senior Member, IEEE) received the B.S. and Ph.D. degrees in electrical and computer engineering from the University of Michigan-Shanghai Jiao Tong University Joint Institute, Shanghai Jiao Tong University, Shanghai, China, in 2012 and 2017, respectively.

He is currently a Research Assistant Professor with the Center for Ultra-Wide-Area Resilient Electric Energy Transmission Networks (CURENT), The University of Tennessee, Knoxville, TN, USA. His research interests include situational awareness, renewable energy source control, optimization, decentralized control of microgrid, and PMU design.

Wei Qiu (Member, IEEE) received the B.Sc. degree in electrical engineering from the Hubei University of Technology, Wuhan, China, in 2015, and the M.Sc. and Ph.D. degrees in electrical engineering from Hunan University, Changsha, China, in 2017 and 2021, respectively.
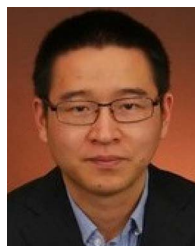
From 2019 to 2021, he was also a joint Doctoral Student with The University of Tennessee, Knoxville, TN, USA, where he is currently a Research Associate with the Department of Electrical Engineering and Computer Science. His current research interests include situational awareness, cyber-security of synchrophasor, and power quality measurement.

Andy Hoke (Senior Member, IEEE) received the B.A. degree in engineering physics from Dartmouth College, Hanover, NH, USA, in 2001, and the M.S. and Ph.D. degrees in electrical engineering from the University of Colorado (UCB), Boulder, CO, USA, in 2013 and 2016, respectively.

In 2014, he was with Power Systems Engineering Center, National Renewable Energy Laboratory (NREL), Golden, CO, where he is currently a Senior Engineer. Prior to that, he was a Graduate Researcher with NREL and a Research Assistant with Colorado Power Electronics Center, UCB, from 2010 to 2014. He has authored and coauthored more than 30 publications. His research interests include power electronics and hardware in the loop for the integration of inverter-based sources with electric power systems.

Dr. Hoke is a Registered Professional Engineer and is currently the Chair of the IEEE P1547.1 Working Group. He was the recipient of the IEEE Power and Energy Society General Meeting Best Conference Paper Awards in 2015 and 2017.

Yuru Wu (Student Member, IEEE) received the B.S.E. degree in electronic engineering from Tsinghua University, Beijing, China, in 2017. He is currently working toward the Ph.D. degree in power electronic engineering from The University of Tennessee, Knoxville, TN, USA.

His research interests include phase measurement unit design, power quality in grid, noise analysis, and algorithm design.

Cameron J. Kruse (Member, IEEE) received the B.S. degree in electrical engineering from the University of Arizona, Tucson, AZ, USA, in 2008.

He is currently a Substation Operations Supervisor with Kauai Island Utility Cooperative, Lihue, HI, USA. His work direction is large-scale renewable integration, substation operations, and power system protection.

Brad W. Rockwell (Member, IEEE) received the B.S. degree in marine engineering from United States Naval Academy, Annapolis, MD, USA, and the MBA degree in finance from the University of Hawaii, Honolulu, HI, USA, in 2014.

He joined Kauai Island Utility Cooperative, Lihue, HI, USA, in 2003, and he has worked for the past 18 years. He is currently the Chief of Operations with Kauai Island Utility Cooperative. His work direction is power supply and operation.

Yilu Liu (Fellow, IEEE) received the B.S. degree from Xi'an Jiaotong University, China, and the M.S. and Ph.D. degrees from The Ohio State University, Columbus, OH, USA, in 1986 and 1989, respectively, all in electrical engineering.

She is currently the Governor's Chair with The University of Tennessee, Knoxville, TN, USA, and Oak Ridge National Laboratory (ORNL), Oak Ridge, TN, USA. She is elected as a member of National Academy of Engineering in 2016. She is also the Deputy Director of the DOE/NSF-cofunded engineering research center CURENT. Prior to joining UTK/ORNL, she was a Professor with Virginia Tech. She led the effort to create the North American power grid Frequency Monitoring Network (FNET), Virginia Tech, which is now operated at UTK and ORNL as GridEye. Her current research interests include power system wide-area monitoring and control, large interconnection-level dynamic simulations, electromagnetic transient analysis, and power transformer modeling and diagnosis.